Article

Influence of Water–Oil Saturation on the Fracture Process Zone: A Modified Dugdale–Barenblatt Model

Yuanxun Nie [1] , **Guangqing Zhang [1,2],*, Yuekun Xing [1,2] and Shiyuan Li [1,2]**

[1]   Department of Engineering Mechanics, China University of Petroleum (Beijing), Beijing 102248, China;
      nieyuanxun@126.com (Y.N.); yuekunxing@gmail.com (Y.X.); lishiyuan1983@cup.edu.cn (S.L.)
[2]   State Key Laboratory of Petroleum Resources and Engineering, Beijing 102248, China
*   Correspondence: zhangguangqing@cup.edu.cn; Tel.: +86-010-8973-3920

check for updates

Abstract: The wetting and nonwetting fluid saturations in porous reservoirs always change during long-term injection and production. The fracture process zone (FPZ) is a prominent feature in the rock fracture process. If the FPZ properties are influenced by pore fluids, the process of hydraulic fracturing will change greatly. The existing models do not consider the role of pore fluid when characterizing the FPZ. In this paper, a modified Dugdale–Barenblatt (D–B) model with capillary pressure is proposed. The model reflects the fact that the FPZ length decreases nonlinearly with the increase in capillary pressure, and it reveals the mechanism of capillary pressure on the equivalent fracture cohesion in the FPZ, which affects the FPZ length. Three-point bending tests were carried out on sandstone under various fluid saturations through digital image correlation (DIC), acoustic emission (AE), and scanning electron microscope (SEM). It was found that the FPZ length of the water–oil-saturated samples was 30–50% smaller than that of water-saturated/oil-saturated samples due to the capillary pressure effect, and the modified D–B model was well consistent with the experiments. The AE behaviors of different saturated samples were not the same: The cumulative AE signals changed abruptly at 90% of the peak load for the water–oil-saturated samples and at 50% of the peak load for water-saturated samples. This demonstrated that the effect of capillary pressure was more obvious than the weakening effect of microstructural damages. The significant influence of capillary pressure on FPZ requires continuous recognition in hydraulic fracturing design.

Keywords: capillary pressure; fracture process zone length; modified Dugdale–Barenblatt model; digital image correlation

1. Introduction

As global energy provided by conventional reservoirs has become more difficult, the development of oil and gas in unconventional reservoirs is increasingly necessary [1]. The wetting and nonwetting fluid saturations in reservoirs always change as a result of long-term injection and production [2]. The fractures produced by hydraulic fracturing and the existing fractures in depleted reservoirs are affected by the water–oil saturation. During hydraulic fracturing, fracture initiation and propagation are closely related to the nonlinear elastic response that occurs in the fracture process zone (FPZ) [3]. Therefore, investigating the effect of water–oil saturation on the FPZ is of great importance for production improvement.

The effect of pore fluids on mechanical properties needs to be taken into consideration during the rock fracture process. Many scholars have performed a series of experiments to research the influence of water content on the mechanical properties of rocks. The results showed that the static Young's modulus [3,4], dynamic Young's modulus [5,6], compressive stress [3,7], tensile stress [4], and fracture toughness [8–10] decreased drastically with the increase in water content. The effect of

pore fluids on the mechanical properties is a complicated process [5], which includes physical–chemical and mechanical effects (such as capillary pressure). Researchers [11–19] have focused on the physical–chemical effects of water on rock strength, such as clay swelling and chemical reactions. Besides, capillary pressure (the pressure difference of wetting and nonwetting fluids) has been shown to increase strength [5] and fracture toughness [9]. When the content of the wetting and nonwetting fluids are different, there are differences in the effects of the physical–mechanical and capillary pressure, which results in different trends in the mechanical properties. The fracture process zone is a prominent feature of the rock fracture process. As the mechanical properties of rocks can be influenced by pore fluids, it is not difficult to speculate that the fracture process zone of rock is closely related to pore fluid saturation.

In addition to studying the effects of pore fluids on mechanical parameters and the fracture process, researchers have proposed various models to describe the FPZ. In 1960, Dugdale [20] found that a plastic zone at the fracture tip was concentrated at an angle of $45°$ to the plane of the mild sheet, and the ribbon yielding model was proposed. In 1962, Barenblatt [21] found that a small nonlinear stress cohesion zone at the fracture tip eliminated stress singularity. Researchers have since combined these two models into the classic Dugdale–Barenblatt (D–B) model, and many modified D–B models have been proposed. Classical FPZ models include the virtual fracture model [22], the passivation model [23], and the equivalent model [24]. All these models assume that strain softening occurs at the fracture tip. The FPZ length can be calculated based on these models. Labuz et al. [25] presented an experimental analysis of fracture growth in dry charcoal granite that incorporated the concept of the process zone, and they proposed a model to calculate the FPZ length. Although many models have been provided, little research has concentrated on the influence of capillary pressure on the FPZ length.

The primary objective of this study was to investigate the influence of capillary pressure on the FPZ length. For this, the authors propose a modified classical D–B model considering capillary pressure. Three-point bending experiments were conducted with digital image correlation (DIC) and acoustic emission (AE) to verify the proposed model. The microstructural variations of different saturated samples were compared with scanning electron microscope (SEM) results.

2. Modified Fracture Process Zone Model

As capillary pressure can increase strength and fracture toughness [5,9] and as the magnitude of capillary pressure is similar to tensile strength [26], the capillary pressure in the fracture tip is a non-neglectable factor during the fracture process. It can be inferred that capillary pressure will have an effect on the FPZ length. However, the influence of capillary pressure on the FPZ length is not considered in classical FPZ models. In this paper, the authors therefore propose a modified Dugdale–Barenblatt model that considers capillary pressure.

2.1. Liquid Bridges between Idealized Grains

When the pores of porous rock are filled with wetting and nonwetting fluids, the liquid bridge between the grains is shown in Figure 1. The liquid bridge force between grains comprises two parts: surface tension from the wetting phase and the capillary pressure formed by the two fluids. The direction of the liquid bridge force points to the center of the two grains.

The liquid bridge force is expressed as in Equation (1) [27]:

$$F = F_{\text{cap}} + F_{\text{surf}} = \frac{2\pi\gamma R_1{}^2(\sin\varphi)^2\cos(\theta+\varphi)}{R_1(1-\cos\varphi)+d} + 2\pi\gamma R_1\sin\varphi\sin(\theta+\varphi) \tag{1}$$

where d (μm) is the half-length between the two grains centers; R_1 (μm) is the grain radius; φ (degree) is the half-filling angle; F_{cap} (N) is the liquid force caused by the capillary pressure; γ (mN/m) is the surface tension of the two phases; F_{surf} (N) is the liquid bridge force caused by the surface tension of the wetting phase fluid; and F (N) is the resultant liquid bridge force.
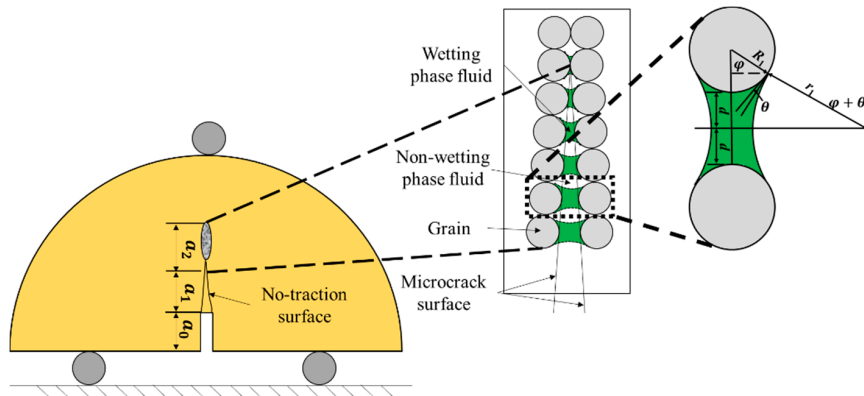
Figure 1. Schematic diagram of pore fluids at the fracture tip.

2.2. Modified FPZ Model

The geometry of a fracture presented in Figure 1 consists of a prefabricated fracture a_0 (mm), a real fracture a_1 (mm), and a microfracture a_2 (mm) as an FPZ [28].

For the modified FPZ model, the authors assumed that the dimension of the fracture process zone was small in comparison with the length of the whole fracture. The grain size of the samples was the same. There was no stress singularity at the tip of the fracture.

The superposition of the stress intensity factors caused by the external load, yield stress, and liquid bridge force at the fracture tip was equal to 0, as shown in Equation (2).

$$K_{\text{tip}} = K_\sigma + K_y + K_F = 0 \tag{2}$$

$$K_F = \frac{-F}{\pi (R_1 \sin \varphi)^2 \sqrt{\pi c}} \left(\int_{-c}^{-a} \sqrt{\frac{c+x}{c-x}} dx + \int_a^c \sqrt{\frac{c+x}{c-x}} dx \right) = \frac{-2\sqrt{c} F \cos^{-1}(a/c)}{\pi^{1.5} (R_1 \sin \varphi)^2} \tag{3}$$

$$\begin{aligned} a &= a_0 + a_1 \\ c &= a_0 + a_1 + a_2 \end{aligned} \tag{4}$$

where K_σ (Pa·m$^{0.5}$), K_y (Pa·m$^{0.5}$), K_F (Pa·m$^{0.5}$), a (mm), c (mm) are the stress intensity factors produced by the external load, the yield stress, the liquid bridge force at the fracture tip, the prefabricated fracture length, and the prefabricated fracture length, respectively. The stress intensity factor produced by the liquid bridge force at the fracture tip can be shown as in Equation (3). The FPZ length with pore fluids can be simplified into Equation (5), and the stress produced by the liquid bridge can be expressed as in Equation (6).

$$l_P = a / \left[8 \left(\frac{\sigma_F}{\sigma} + \frac{\sigma_s}{\sigma} \right)^2 - \pi^2 \right] \tag{5}$$

$$\sigma_F = \left(\frac{2\pi \gamma R_1{}^2 (\sin \varphi)^2 \cos(\theta + \varphi)}{R_1(1 - \cos \varphi) + d} + 2\pi \gamma R_1 \sin \varphi \sin(\theta + \varphi) \right) / (\pi (R_1 \sin \varphi)^2) \tag{6}$$

where l_P (mm) is the FPZ length, and σ_F (MPa) is the stress produced by the liquid bridge. As shown in Equation (5), the formulation to determine the FPZ length will change when the capillary pressure exists.

2.3. Estimating the Influence of Capillary Pressure on an Idealized Sample

In order to quantify the influence of capillary pressure on FPZ length, the authors assumed that the grain radius R_1, the contact angle θ, the surface tension γ of the water and oil, and the peak load were 25 μm, 13° [29], 36 mN/m [30], and 0.8 kN, respectively. For simplification, the relationship between φ and d was assumed to be linear. It was assumed that when the largest filling angle was 60°, the corresponding length between the grains was 20 μm; when the smallest filling angle was 30°,

the corresponding length between the grains was 0.1 μm. This linear relationship can be expressed as in Equation (7).

$$d = 4.5(60° - \varphi) \tag{7}$$

where d (μm) is the half-length between the two grains centers, and φ (degree) is the half-filling angle.

As the half-filling angle is not constant in reality, two extreme cases for simplification were assumed, i.e., that all the filling angles were either 30° or 60°. Based on this assumption, the authors obtained the corresponding FPZ length, and the true length was between the maximum and the minimum. According to Equation (5), the decrease in FPZ length could be up to 30% due to the influence of capillary pressure because the FPZ length decreased by 30% and 5% compared with the dry sample for filling angles of 30° and 60°, respectively.

3. Samples and Methods

3.1. Sample Preparation

Due to the relative uniformity in diameter of the particles and the homogeneity of the mechanical properties, sandstone was selected as the samples, with an average grain diameter in the range of 25–100 μm, uniaxial compressive strength of 70 MPa, tensile strength of 7 MPa, elastic modulus of 8 GPa, porosity of 15%, and Poisson's ratio of 0.2. The X-ray diffraction (XRD) analysis found the average mineral contents, which are listed in Table 1. I/S, S, and K represent illite/smectite, smectite, and kaolinite, respectively.

Table 1. Characterization of the minerals in the samples.

Minerals	SiO$_2$ (%)	S/I (%)	S (%)	K (%)
Content	93.20	1.84	0.54	4.42

Following the International Society for Rock Mechanics and Rock Engineering (ISRM) test standard [31], the samples were cut into semicircular plates with prefabricated fractures in the center. The dimensions of the samples are shown in Table 2, where a (mm) represents the length of the prefabricated fracture, R (mm) represents the radius of the samples, and B (mm) represents the thickness of samples. After processing the samples, the fluid saturating treatments [19] were conducted. Firstly, the dry sample was placed in a sealed container, which was then evacuated. Secondly, the saturated fluid was injected into the container under the negative pressure produced by the vacuum. Finally, the sample was saturated in the fluids for two months so that the oil/water molecules moved into the small pores. The saturating fluids were water and kerosene. For sandstone, water was the wetting fluid, while kerosene was the nonwetting fluid.

Table 2. Specific dimensions of the samples.

Conditions	No.	a (mm)	R (mm)	B (mm)
Dry	D-1	9.910	49.75	28.27
	D-2	9.360	49.76	27.00
	D-3	10.60	49.65	27.70
	D-4	9.806	49.37	28.41
Water-Saturated	W-1	9.270	49.76	28.38
	W-2	10.80	48.44	28.22
	W-3	9.532	49.38	28.21
Oil-Saturated	O-1	10.40	48.20	28.38
	O-2	10.04	49.52	28.14
Water–Oil-Saturated	C-1	9.892	49.62	28.03
	C-2	9.672	49.78	28.01

For DIC, artificial speckles needed to be made on the surface of the sample. After the saturating treatments, one surface was sealed with paraffin and the other was painted with a thin layer of matte white paint to create a white base film, which was facing the camera. Then, a matte black paint was applied to make speckles. For high-quality specks, matte white and black paint should be sprayed alternately.

3.2. Experimental Equipment and Methods

The experimental devices are illustrated in Figure 2, where DIC and AE were used to record the fracture process. Internal damages to the rock during the fracture process are due to the change of the microstructure [32–34] and are detected by AE [35]. The DIC technology can be used to obtain the deformation of the grains on the surface [36–39].

To calculate the FPZ length from the displacement [36], DIC technology was deployed during the fracture process. Speckles were located and recorded under loading through a charge-coupled device (CCD) high-speed camera with an effective pixel of 2062×2062, a 35 mm fixed focus lens, and a high-speed capacity at a rate of two frames/s. The width and height of the camera window view focused on the 50 mm on both sides of the prefabricated fractures and 40 mm at the top of the prefabricated fracture, respectively. A stabilized white light source was used for a better light effect. As shown in Figure 2a, there were four sensors arranged on the light source side and the back side. The AE signal acquisition device was a SAEU2S-centralized AE system, and the threshold was 40 dB.

The load was applied with a hydraulic servo control system at the rate of 0.1 mm/min. Simultaneous recording of the AE signals (AE energy, amplitude, hit count, and the arrival time of signals) and high-speed camera were carried out until the whole fracture process was completed.
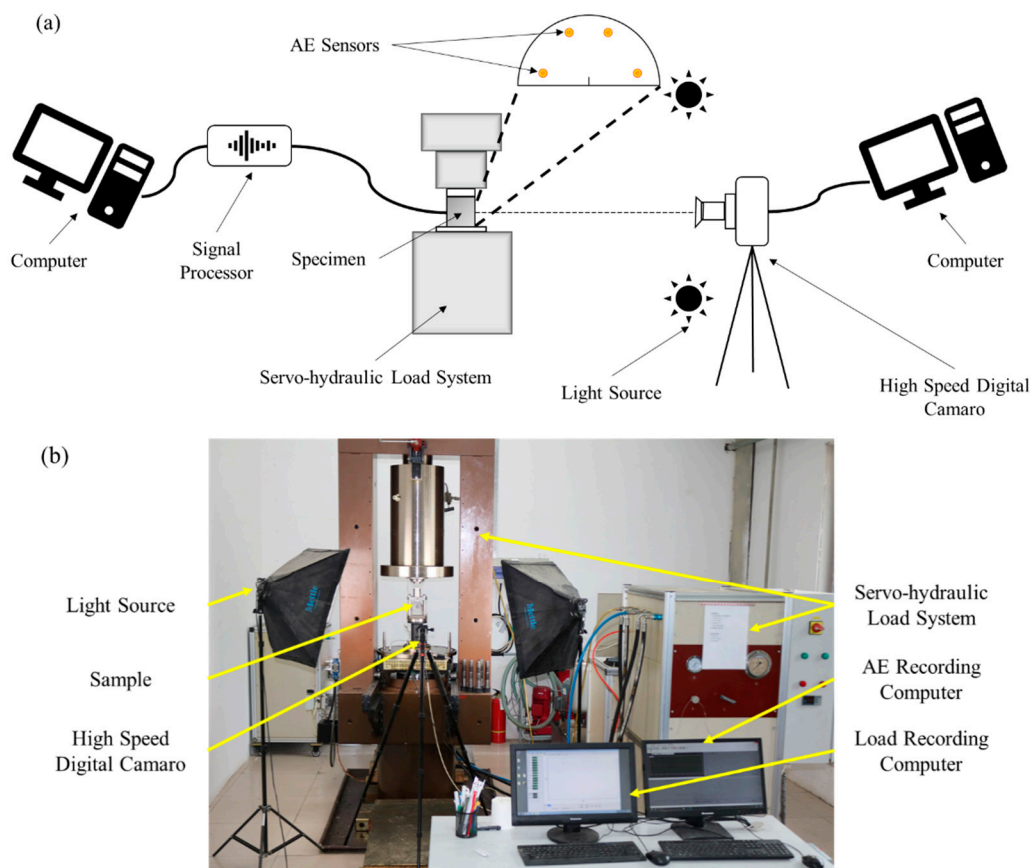

Figure 2. Digital image correlation system: (**a**) Schematic diagram; (**b**) Equipment photo.

3.3. Determination of FPZ Length

Under an external load, the initiation and propagation of a microfracture will lead to an increase in the fracture tip displacement. The fracture extends unstably only when the crack tip opening displacement (CTOD) reaches the critical value. For tight rocks, the fracture propagates unstably at the peak load, and the zone in front of prefabricated fracture can be defined as the FPZ.

Figure 3 shows that the incremental horizontal displacement contours merge at one point, which is defined as the FPZ tip [36]. At the peak load, the FPZ length is defined to be the distance between the merged point and the tip of the prefabricated fracture. The exact definition of the merged point is closely correlated with the size of the FPZ. There are different material properties inside and outside the FPZ. The deformation characteristics in those regions are different, and the position where the slope of incremental displacement abruptly changes is defined to be the merged point [36]. As shown in Figure 4, the horizontal displacements at the peak load of $y = 0$, $y = 2.47$ mm, $y = 4.93$ mm, and $y = 5.32$ mm were selected for the dry sample. It was not difficult to find that the displacement profiles of $y = 0$, $y = 2.47$ mm, $y = 4.93$ mm had the same characteristics; the slope could clearly be divided into three sections. However, the slope of the incremental horizontal displacement profile at $y = 5.32$ mm was nearly the same, which indicated that the slope abruptly changed at $y = 4.93$ mm. The corresponding point where the slope changed was defined as the merged point.
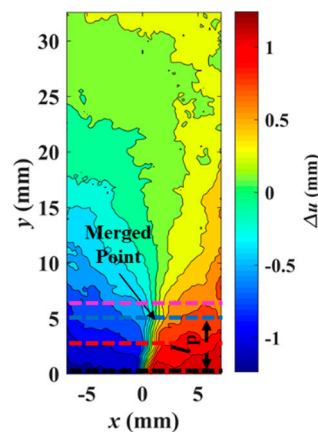

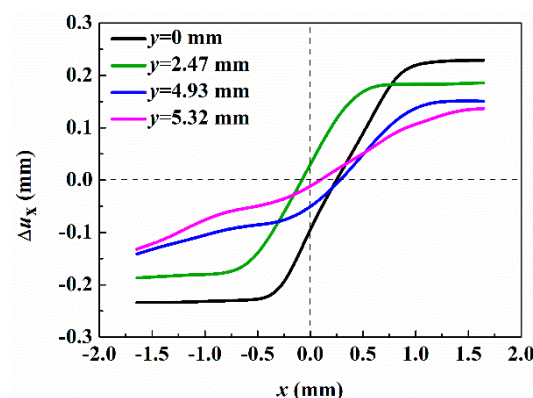**Figure 3.** Incremental horizontal displacement contours of the dry sample.

Figure 4. Dry sample: peak and incremental horizontal displacement profiles.

4. Results and Discussion

In the following section, the influence of capillary pressure on the FPZ length is discussed based on the measurement of the FPZ length according to DIC and the combined damage data from the AE.

4.1. Capillary Pressure Decreases FPZ Length

As stated in the previous section, FPZ length can be represented as the distance—along with the prefabricated fracture—between the initial position and the merged point, whose coordinates are specified with DIC at peak loads. For the dry, water-saturated, oil-saturated, and the water–oil-saturated samples, Figures 3 and 5–7 show the contours of the incremental horizontal displacements, respectively. Based on the method described in Section 3.3, the FPZ lengths for the samples with various saturations were obtained, as seen in Figure 8.

Capillary pressure can reduce the FPZ length. The average FPZ length of the water–oil-saturated samples was 3.32 mm—the shortest of all the samples—and was about 15–25 times the grain radius. The lengths of the FPZ for the oil-saturated, dry, and water-saturated samples were about 33%, 63%, and 110% larger than that of the water–oil-saturated sample, respectively. The capillary pressure only existed in the water–oil-saturated samples, thus it can be concluded that capillary pressure decreased the FPZ length.

Water–oil saturation can affect the pore structure of the sample and the cohesive strength of the grains. The changes in the microstructure of different saturated samples were observed by SEM in order to describe the influence of different types of pore fluids; the results are described in the following sections. Combined with the analysis of the forces between the grains, the influence of capillary pressure on FPZ length is then discussed.
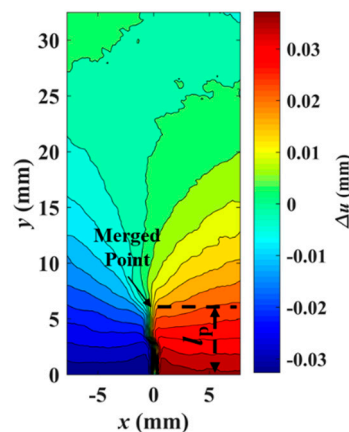

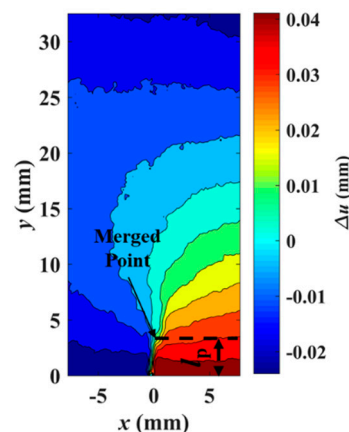**Figure 5.** Incremental horizontal displacement contours of water-saturated sample.

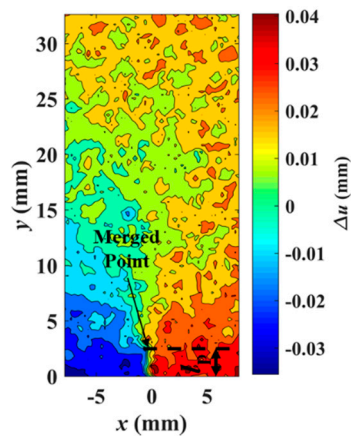**Figure 6.** Incremental horizontal displacement contours of oil-saturated sample.

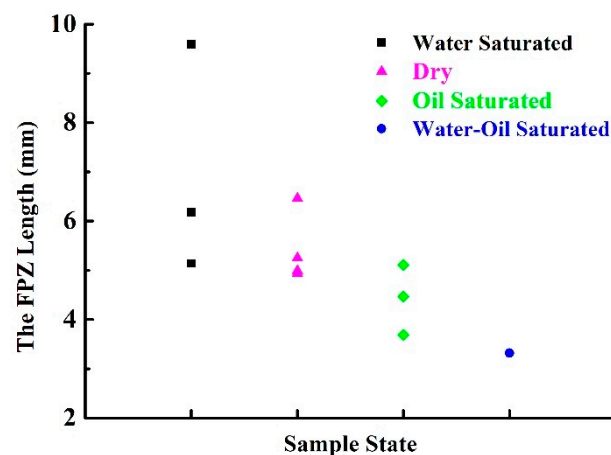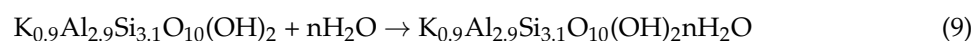**Figure 7.** Incremental horizontal displacement contours of water–oil-saturated sample.
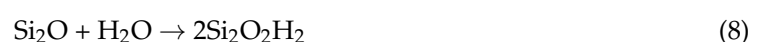

Figure 8. The fracture process zone (FPZ) length vs. sample state.

4.2. Capillary Pressure Affects FPZ More than Microstructural Damages

The FPZ length of the water-saturated samples was the longest due to the damaging effect of the water–rock reaction on the microstructure. Some swelling, dissolution, and cementitious mineral loss always occur as a result of the existence of pore fluids [10], which weakens the ability to sustain the load. Figure 9a–c show the microstructures of the dry sample, and there were some flaky and floccular minerals among the grains. The composition of the constituent elements of these minerals, as found by the SEM analysis, are shown in Figure 10. According to Figure 10, the significant presence of Al was an indication of the presence of aluminosilicate, which can react with water as shown in Equations (8) and (9) [40]. The reaction led to mineral loss among the grains, which weakened the cementation; the microstructure of the sample then became the type shown in Figure 9d, and there were many microfractures among the grains. Figure 9e,f show the microstructure of the oil-saturated and water–oil-saturated samples, respectively. In Figure 9, it can be seen that the water-saturated sample had the most microfractures, and the water–oil-saturated sample was slightly affected; however, the microstructure of the oil-saturated sample was almost unaffected. This showed that the change in the microstructure was one of the reasons for the longer length of the FPZ in the water-saturated sample.

$$Si_2O + H_2O \rightarrow 2Si_2O_2H_2 \tag{8}$$

$$K_{0.9}Al_{2.9}Si_{3.1}O_{10}(OH)_2 + nH_2O \rightarrow K_{0.9}Al_{2.9}Si_{3.1}O_{10}(OH)_2nH_2O \tag{9}$$

The attraction between the grains at the fracture tip due to the liquid bridge force from the capillary pressure was stronger than the weakening effect of the microstructural damages. As sandstone is a porous medium, pore fluids can produce a liquid bridge, which produces a liquid bridge force

that resists particle separation. The liquid bridge force (especially capillary pressure) can strengthen the cohesion between particles. Although the damage to the water–oil-saturated samples was more serious than that of the oil-saturated samples, the length of the FPZ of the water–oil-saturated sample was smaller than that of the oil-saturated sample shown in Figure 8, which indicated that hydration reaction played a less important role than capillary pressure.
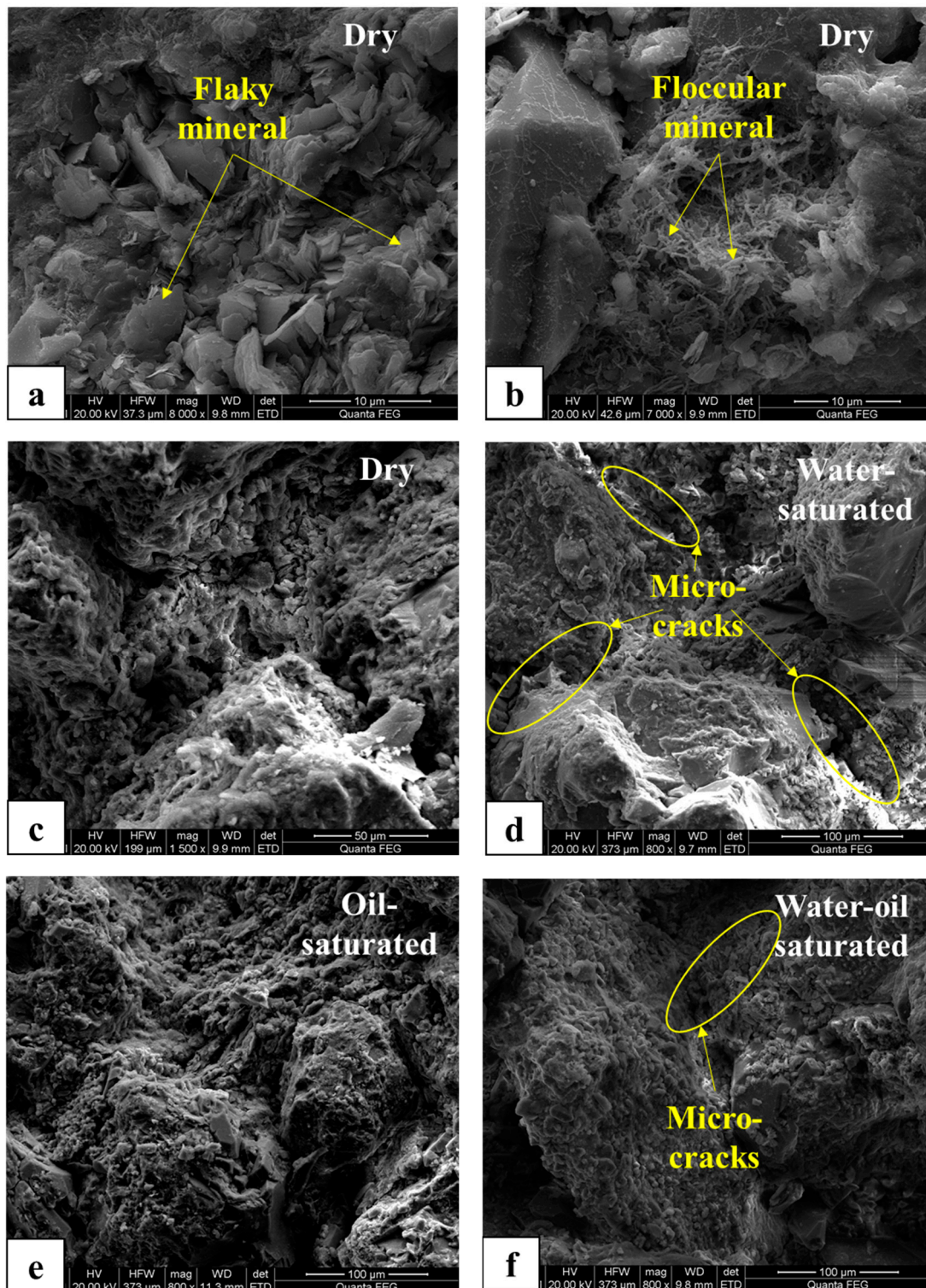

Figure 9. Scanning electron microscope (SEM) images of different saturated samples: (**a**–**c**) Dry sample; (**d**) Water-saturated sample; (**e**) Oil-saturated sample; (**f**) Water–oil-saturated sample.
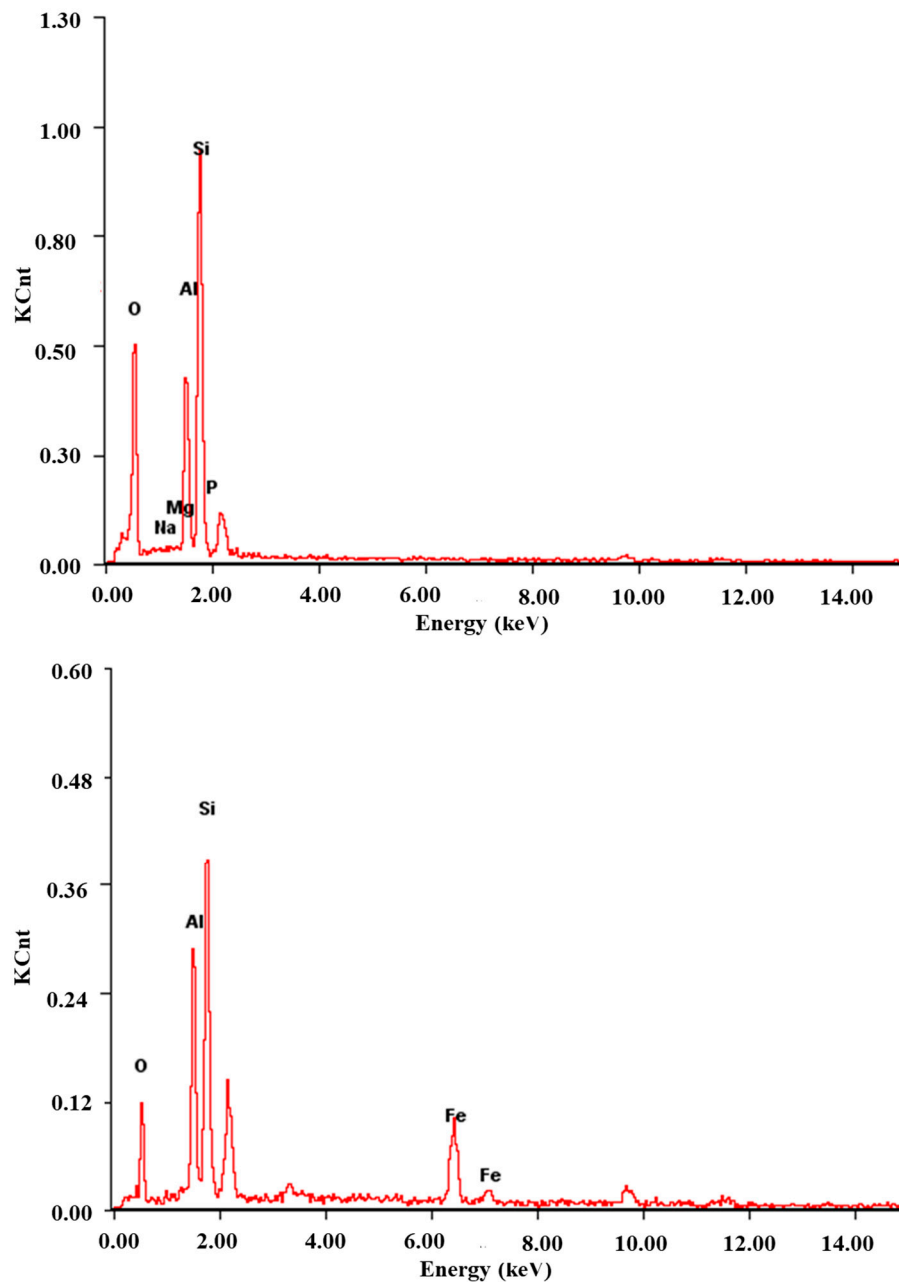
Figure 10. Composition of the elements in the sandstone sample, as found by SEM tests.

4.3. Acoustic Emission Characteristics Affected by Water–Oil Saturation

Different saturated samples showed different AE behavior, which could be described from two aspects: the cumulative AE hit count and the AE cumulative energy [41,42].

The damage caused by water was the greatest of all the saturation scenarios. The cumulative AE hit count describes the damage magnitude of the sample with different water–oil saturations. If the damage is more serious, the significant cumulative hit count occurs earlier. The blue line in Figures 11 and 12 show typical curves for the cumulative AE hit count for the water-saturated sample (W-2) and the water–oil-saturated sample (W-O-1). The cumulative AE signals changed abruptly at 90% of the peak load for the water–oil-saturated samples; this change occurred at 50% of the peak load for the water-saturated samples.

The cohesion of the water-saturated samples was the weakest of all the samples. The AE cumulative energy can represent the strength of the sample with different water/oil contents. When the

cohesion is weak, the energy needed is low. The green line in Figures 11 and 12 shows the cumulative energy over time for the water-saturated sample (W-2) and the water–oil-saturated sample (W-O-1). It was evident that the energy released from the water–oil-saturated sample was about 5 times that of the water-saturated sample. It was shown that the cohesion between the grains in the water-saturated sample was weaker than that of the water–oil-saturated samples. When the cohesion was weaker, the FPZ length was larger, which was well consistent with the modified model.
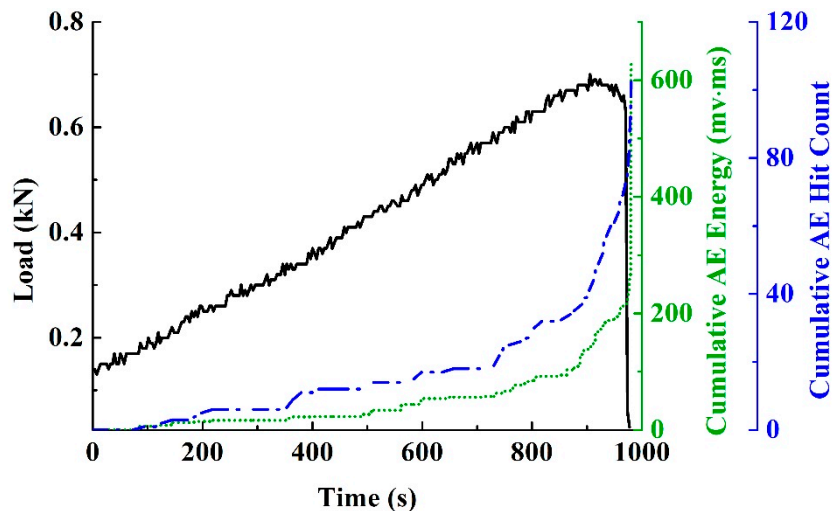

Figure 11. The cumulative acoustic emission (AE) energy and cumulative AE hit count of the water-saturated sample (W-2).
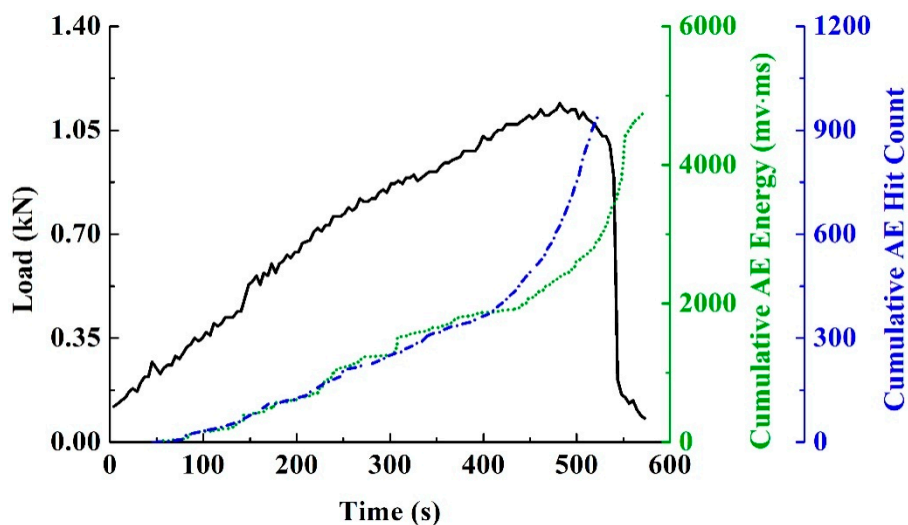

Figure 12. The cumulative AE energy and cumulative AE hit count of the water–oil-saturated sample (W-O-1).

4.4. Impact on Engineering Design

Drawing on the above discussion, it is not difficult to find that capillary pressure reduced the FPZ length. This may be of benefit to modify the design of hydraulic fracturing.

During the process of designing hydraulic fractures, engineers always set the volume of the injected liquid to control the length of the hydraulic fracture. However, capillary pressure is always neglected. Due to capillary pressure, the fracture toughness is higher than that obtained in the lab, and the actual length of the fracture may be shorter than the designed one. The design length of the fracture should be longer than the designed one. This may be one of the reasons for the low production.

5. Conclusions

In this paper, the influence of water–oil saturation on the FPZ was studied by means of capillary pressure and the weakening effect of microstructural damages. More attention was paid to the influence of capillary pressure. The FPZ is a prominent feature in the rock fracture process. However, existing models do not consider the role of pore fluid when characterizing the FPZ. In this study, a modified Dugdale–Barenblatt (D–B) model with capillary pressure is therefore proposed. The model reflects the fact that the FPZ length decreases nonlinearly with the increase in capillary pressure, and it reveals the mechanism of capillary pressure on the equivalent fracture cohesion in the FPZ, which affects the FPZ length. Three-point bending tests were carried out on sandstone under various fluid saturations. It was found that the FPZ length of the water–oil-saturated samples was 30–50% smaller than that of the water-saturated/oil-saturated samples due to the capillary pressure effect; the modified D–B model was well consistent with the experiments. The AE behaviors of the different saturated samples were not the same: The cumulative AE signals changed abruptly at 90% of the peak load for water–oil-saturated samples; this change occurred at 50% of the peak load for the water-saturated samples. This demonstrated that the effect of capillary pressure was more obvious than the weakening effect of the microstructural damage. This research will be beneficial for understanding the fracture process in reservoirs, where the saturations of wetting and nonwetting fluids always change.

References

1. Altwaijri, M.; Xia, Z.H.; Yu, W.; Qu, L.C.; Hu, Y.P.; Xu, Y.F.; Sepehrnoori, K. Numerical study of complex fracture geometry effect on two-phase performance of shale-gas wells using the fast EDFM method. *J. Petrol. Sci. Eng.* **2018**, *164*, 603–622. [CrossRef]

2. Duan, S.; Li, X.; Wojtanowicz, A.K. Dynamic growth of water saturation around oil wells by water coning and transverse dispersion. *J. Petrol. Sci. Eng.* **2011**, *78*, 447–453. [CrossRef]

3. Atkinson, B.K. *Fracture Mechanics of Rock*, 1st ed.; Academic Press: New York, NY, USA, 1987; p. 262.

4. Dowla, N.; Hayatdavoudi, A.; Ghalambor, A.; Okoye, C.; Alcocer, C. Laboratory investigation of saturation effect on mechanical properties of rocks. In Proceedings of the SPWLA 31st Annual Logging Symposium, Lafayette, LA, USA, 24–27 June 1990; Society of Petrophysicists and Well Log Analysts: Houston, TX, USA, 1990.

5. Lai, B.T.; Li, H.; Zhang, J.L.; Jacobi, D.; Dan, G. Water content effects on dynamic elastic properties of organic rich shale. *SPE J.* **2016**, 1–13. [CrossRef]

6. Han, D.; Batzle, M. Gassmann's Equation and Fluid-Saturation Effects on Seismic Velocities. *Geophysics* **2004**, *69*, 398–405. [CrossRef]

7. Vásárhelyi, B.; Ván, P. Influence of water content on the strength of rock. *Eng. Geol.* **2006**, *84*, 70–74. [CrossRef]

8. Nara, Y.; Morimoto, K.; Hiroyoshi, N.; Yoneda, T.; Kaneko, K.; Benson, P.M. Influence of Relative Humidity on Fracture Toughness of Rock: Implications for Subcritical Fracture Growth. *Int. J. Solids Struct.* **2012**, *49*, 2471–2481. [CrossRef]

9. Nie, Y.X.; Zhang, G.Q.; Tang, M.R.; Zhao, B.; Pan, R.; Liu, Z.B.; Xu, S.F.; Yang, X. Effect of Water-oil Saturation on Fracture Toughness of Reservoir Rocks During Long-term Production. In Proceedings of the 51st U.S. Rock Mechanics/Geomechanics Symposium, San Francisco, CA, USA, 25–28 June 2017.

10. Hua, W.; Dong, S.M.; Li, Y.F.; Xu, J.; Wang, Q.Y. The Influence of Cyclic Wetting and Drying on the Fracture Toughness of Sandstone. *Int. J. Rock Mech. Min.* **2015**, *78*, 331–335. [CrossRef]

11. Koji, M. Effects of water on rock strength in a brittle regime. *J. Struct. Geol.* **2001**, *23*, 1653–1657. [CrossRef]

12. Wong, L.N.Y.; Maruvanchery, V.; Liu, G. Water effects on rock strength and stiffness degradation. *Acta Geotech.* **2015**, *11*, 713–737. [CrossRef]

13. Li, D.Y.; Wong, L.N.Y.; Liu, G.; Zhang, X.P. Influence of water content and anisotropy on the strength and deformability of low porosity meta-sedimentary rocks under triaxial compression. *Eng. Geol.* **2012**, *126*, 46–66. [CrossRef]

14. Wang, L.L.; Zhang, G.Q.; Hallais, S.; Tanguy, A.; Yang, D.S. Swelling of shales: A multiscale experimental investigation. *Energy Fuels* **2017**, *31*, 10442–10451. [CrossRef]

15. Dehghanpour, H.; Zubair, H.A.; Chhabra, A.; Ullah, A. Liquid intake of organic shales. *Energy Fuels* **2012**, *26*, 5750–5758. [CrossRef]

16. Dehghanpour, H.; Lan, Q.; Saeed, Y.; Fei, H.; Qi, Z. Spontaneous imbibition of brine and oil in gas shales: Effect of water adsorption and resulting microfractures. *Energy Fuels* **2013**, *27*, 3039–3049. [CrossRef]

17. Atkinson, B.K.; Meredith, P.G. Stress corrosion cracking of quartz: A note on the influence of chemical environment. *Tectonophysics* **1981**, *77*, T1–T11. [CrossRef]

18. Zhang, Y.H.; Lebedev, M.; Al-Yaseri, A.; Yu, H.; Xu, X.; Sarmadivaleh, M.; Barifcani, A.; Iglauer, S. Nanoscale rock mechanical property changes in heterogeneous coal after water adsorption. *Fuel* **2018**, *218*, 23–32. [CrossRef]

19. Zhao, B.; Zhang, G.Q.; Zhao, P.Y.; Wang, L.L.; Lin, Y.; Lv, Y.J. Experimental study of mechanics and seepage characteristics of sandstones after liquid-nitrogen stimulation. *J. Nat. Gas Sci. Eng.* **2017**, *47*, 11–21. [CrossRef]

20. Dugdale, D.S. Yielding of Steel Sheets Containing Slits. *J. Mech. Phys. Solids* **1965**, *5*, 100–104. [CrossRef]

21. Barenblatt, G.I. The Mathematical Theory of Equilibrium Cracks in Brittle Fracture. *Adv. Appl. Mech.* **1962**, *7*, 55–129. [CrossRef]

22. Hilerborg, A.; Modéer, M.; Petersson, P.E. Analysis of Crack Formation and Crack Growth in Concrete by Means of Fracture Mechanics and Finite Elements. *Cem. Concr. Res.* **1976**, *6*, 773–782. [CrossRef]

23. Bažant, Z.P. Mechanics of Distributed Cracking. *Appl. Mech. Rev.* **1986**, *39*, 675–705. [CrossRef]

24. Jenq, Y.S.; Shan, S.P. A Fracture Toughness Criterion for Concrete. *Eng. Fract. Mech.* **1985**, *5*, 1055–1069. [CrossRef]

25. Labuz, J.F.; Shan, S.P.; Dowding, C.H. Experimental analysis of crack propagation in granite. *Int. J. Rock. Mech. Min. Sci. Geomech. Abstr.* **1985**, *22*, 85–98. [CrossRef]

26. Schubert, H. Tensile strength and capillary pressure of moist agglomerates. *Agglomeration* **1977**, *77*, 144–155.

27. Hotta, K.; Takeda, K.; Linoya, K. The capillary binding force of a liquid bridge. *Power Technol.* **1974**, *10*, 231–242. [CrossRef]

28. Zhang, D.; Wu, K. Fracture Process Zone of Notched Three-point-bending Concrete Beams. *Cem. Concr. Res.* **1999**, *29*, 1887–1892. [CrossRef]

29. Kaveh, N.S.; Rudolph, E.S.J.; Hemert, P.V.; Rossen, W.R.; Wolf, K.H. Wettability Evaluation of a CO2/Water/Bentheimer Sandstone System: Contact Angle, Dissolution, and Bubble Size. *Energy Fuels* **2014**, *28*, 4002–4020. [CrossRef]

30. Pavitran, S.; Balasubramanian, S.; Kumar, P.; Bisen, P.S. Emulsification and utilization of high-speed diesel by a Brevibacterium species isolated from hydraulic oil. *World J. Microbiol. Biotechnol.* **2004**, *20*, 811–816. [CrossRef]

31. Kuruppu, M.D.; Obara, Y.; Ayatollahi, M.R.; Chong, K.P.; Funatsu, T. ISRM-suggested method for determining the mode-I static fracture toughness using semi-circular bend specimen. *Rock Mech. Rock Eng.* **2014**, *47*, 267–274. [CrossRef]

32. Fakhimi, A.; Galouei, M. Size Effect on Length and Width of Fracture Process Zone. In Proceedings of the 49th US Rock Mechanics/Geomechanics Symposium, San Francisco, CA, USA, 28 June 28–1 July 2015.

33. Koji, O.; Hidehumi, D. Fracture Process Zone in Concrete Tension Specimen. *Eng. Fract. Mech.* **2000**, *65*, 111–131. [CrossRef]

34. Maji, A.; Shan, S. Process Zone and Acoustic-Emission Measurements in Concrete. *Exp. Mech.* **1988**, *28*, 27–33. [CrossRef]

35. Moradian, Z.A.; Ballivy, G.; Rivard, P.; Gravel, C.; Rousseau, B. Evaluating damage during shear tests of joints using acoustic emissions. *Int. J. Rock Mech. Min.* **2010**, *47*, 590–598. [CrossRef]

36. Lin, Q.; Labuz, J.F. Identifying quasi-brittle facture by AE and Digital Imaging. *J. Acoust. Emiss.* **2011**, *29*, 68–77.

37. Lin, Q.; Yuan, H.N.; Biolzi, L.; Labuz, J.F. Opening and Mixed Mode Fracture Process in a Quasi-Brittle Material via Digital Imaging. *Eng. Fract. Mech.* **2014**, *131*, 176–193. [CrossRef]

38. Zang, A.; Wagner, F.C.; Stanchits, S.; Janssen, C.; Dresen, G. Fracture Process Zone in Granite. *J. Geophys. Res.* **2000**, *105*, 23651–23661. [CrossRef]

39. Fakhimi, A.; Lin, Q.; Labuz, J.F. Insights on Rock Fracture from Digital Imaging and Numerical Modeling. *Int. J. Rock Mech. Min.* **2018**, *107*, 201–207. [CrossRef]

40. Atkinson, B.K. Subcritical crack growth in geological materials. *J. Geophys. Res.* **1984**, *89*, 4077–4114. [CrossRef]

41. Sirdesai, N.N.; Gupta, T.; Singh, T.N.; Ranjith, P.G. Studying the Acoustic Emission Response of an Indian Monumental Sandstone under Varying Temperature and Strains. *Constr. Build. Mater.* **2018**, *168*, 346–361. [CrossRef]

42. Lin, Q.; Mao, D.T.; Wang, S.; Li, S.Y. The Influences of Mode II Loading on Fracture Process in Rock Using Acoustic Emission Energy. *Eng. Fract. Mech.* **2018**, *194*, 136–144. [CrossRef]